RESEARCH ARTICLE

Macromolecular Materials and Engineering
Open Access
www.mame-journal.de

Investigating Dynamic Changes in 3D-Printed Covalent Adaptable Polymer Networks

*Yixuan Jia, Christoph A. Spiegel, Juliane Diehm, Daniel Zimmermann, Birgit Huber, Hatice Mutlu, Matthias Franzreb, Manfred Wilhelm, Patrick Théato, Eva Blasco, and Manuel Tsotsalas**

3D printing technologies have matured to produce complex structures, still they are often limited to static materials. Introducing alkoxyamine bonds into 3D printed structures offers unprecedented possibilities for post-synthetic modification through nitroxide exchange reaction and nitroxide-mediated polymerization. This study provides a comprehensive molecular and macroscopic characterization of 3D-printed alkoxyamine-containing dynamic covalent adaptable networks. The study provides new insights into their dynamic structural and mechanical alterations, making them promising candidates for advanced applications ranging from biomedical engineering to flexible electronics.

1. Introduction

3D printing technology, especially digital light processing (DLP), has revolutionized the fabrication of polymer structures with various optical, mechanical, and biological properties.[1–6] However, these advancements often produce static structures, lacking any controlled dynamic properties. The introduction of dynamic covalent bonds and dormant initiator sites,[7,8] which respond to various stimuli, opens up a wide range of advanced applications, including active motion, drug delivery, tissue engineering, and biosensing.[1,3,9] Such modifications at the molecular level present new opportunities for modifying the molecular structure of the networks, including cross-linking density, monomer composition, density, and mesh size[10–13] that can significantly impact the mechanical properties, swelling degree, and guest-molecule accessibility of the polymer networks.[14–17] Inclusion of alkoxyamine bonds within polymer networks offers the unique possibility to act both as a dynamic covalent bond and as a dormant initiator site.[18–22] While work has been done on creating alkoxyamine containing 3D structures in micro-scale and bulk formats,[15,16] the focus of this study lies in meso-scale 3D printing of alkoxyamine-containing dynamic covalent adaptable networks (CANs). By employing an optimized ink formulation that includes nitroxide functional groups, photoinitiator bis(2,4,6-trimethylbenzoyl)-phenyl-phosphine-oxide (Irg819), and the cross-linker poly(ethylene glycol) diacrylate (PEG-DA, M_n = 700 $gmol^{-1}$), we successfully fabricated 3D structures with the unique feature of alkoxyamine bonds (**Figure 1**). These alkoxyamine bonds set the stage for remarkable post-printing modifications enabled by nitroxide exchange reactions (NER) and nitroxide-mediated polymerization (NMP).[23–25] As a result, our approach introduces a new dimension to 3D printing, enabling us to fabricate polymer networks with dynamically tunable shape and composition at both molecular and mesoscopic levels. The resulting polymer networks possess properties such as stimuli-responsiveness and reversible bond formation capabilities.

In a previous study focused on covalent adaptable microstructures (CAMs), we prepared the network in micro-scale using a two photon laser printing technique.[16] This methodology enabled the synthesis of CANs containing dynamic bonds at the micro-scale, allowing manipulation of mechanical properties and microstructure volume. However, when considering the scale of the final 3D microstructure, the available options for characterization methods were limited, due to the small sample amount. In this present study, we offer extensive characterization to understand the mechanical and structural properties of

Y. Jia, J. Diehm, M. Franzreb, M. Tsotsalas
Institute of Functional Interfaces (IFG)
Karlsruhe Institute of Technology (KIT)
76344 Eggenstein-Leopoldshafen, Germany
E-mail: manuel.tsotsalas@kit.edu
C. A. Spiegel, E. Blasco
Institute for Molecular Systems Engineering and Advanced Materials (IMSEAM)
Heidelberg University
69120 Heidelberg, Germany
D. Zimmermann, M. Wilhelm
Institute for Chemical Technology and Polymer Chemistry (ITCP)
Karlsruhe Institute of Technology (KIT)
76131 Karlsruhe, Germany
B. Huber, H. Mutlu, P. Théato
Soft Matter Synthesis Laboratory
Karlsruhe Institute of Technology (KIT)
76344 Eggenstein-Leopoldshafen, Germany
H. Mutlu
Institut de Science des Matériaux de Mulhouse
UMR 7361 CNRS/Université de Haute Alsace
15 rue Jean Starcky, Mulhouse Cedex 68057, France
The ORCID identification number(s) for the author(s) of this article can be found under https://doi.org/10.1002/mame.202300438

DOI: 10.1002/mame.202300438

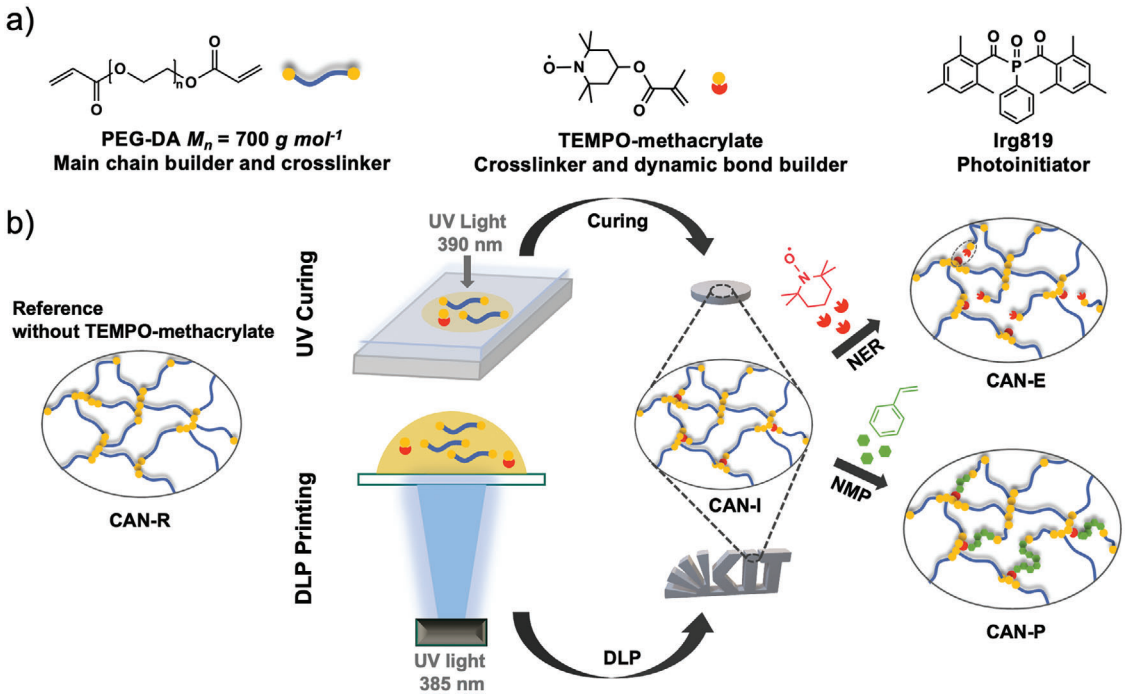

Figure 1. a) Molecular composition of ink employed in digital light processing (DLP) and UV curing; b) Schematic illustration of UV curing and DLP printing for mesoscopic 3D structures, followed by thermal post-synthetic modification of covalent adaptable networks (CANs).

the alkoxyamine-modified structures. For instance, we utilized the characteristic of nitroxide radicals that are electron paramagnetic resonance (EPR) active to follow the dynamic changes in crosslinking density of the polymer networks.[14,15,26,27] Additionally, inverse size-exclusion chromatography (ISEC) was conducted.[15,28–31] By performing size-exclusion chromatography (SEC) in inverse mode, we were able to determine the mesh size distribution of the network. This in-depth analysis elucidates how the unique attributes of alkoxyamine bonds open up possibilities for developing more complex, adaptable, and dynamic materials in the field of 3D printing.

2. Results and Discussion

2.1. Ink Formulation and 3D Structure Curing

The ink formulation is based on work by Torkelson and coworkers[21] and by our previous manuscript on microscale printing.[16] The ink is composed of poly(ethylene glycol) diacrylate (PEG-DA) and TEMPO-methacrylate. To adapt our system to UV curing and DLP curing, we chose Irg819 (see Figure 1a for the chemical structure) as the photoinitiator because it is a well-known and commercially available photoinitiator with excellent initiation properties as demonstrated in various published inks.[32–34] Also, Irg819 exhibits ideal photosensitivity within the 360–400 nm range,[35] which impeccably aligns with the 385 nm DLP curing wavelength. A solvent was needed to fully dissolve the ink system, which includes the nitroxide radical source, photoinitiator, and cross-linker unit. We investigated and tested several high boiling point solvents such as dimethylsulfoxide (DMSO, T_b = 189 °C), dimethylformamide (DMF, T_b = 153 °C), diethylformamide (DEF, T_b = 178 °C), and dimethylacetamide (DMAc, T_b = 165 °C). Except for DMSO, cross-linker PEG-DA and nitroxide source are readily soluble in all of these solvents. When compared to other solvents, DMAc exhibited the best performance in terms of photoinitiator solubility (see Table S2, Supporting Information). In addition, the ink with nitroxide source, PEG-DA as crosslinker and Irg819 could be dissolved in high concentrations using DMAc, leading to the final decision to employ DMAc as solvent. Initial printing tests showed excellent printability, allowing a fast printing process while maintaining well defined 3D structure, which continued to support this strategy.

Once we identified the appropriate ink components, we optimized the ratio between the photoinitiator (Irg819) and the nitroxide source. We recognized that an excessive amount of nitroxide source in comparison to photoinitiator would diminish the quality of the UV curing and printing process, necessitating lower printing speeds and greater exposure energy. Therefore, we considered this ratio to be a critical ink parameter for effective curing or printing. To screen this parameter, we employed a homemade UV curing system (see details in Section S4, Supporting Information) and a commercial DLP printer outfitted with a high-power UV-LED with a wavelength of 385 *nm*. Table S3 (Supporting Information) provides additional information about the optimization of ink compositions. We determined that curing intensities of 12.0 $mWcm^{-2}$ for UV curing and 30.0 $mWcm^{-2}$ for DLP printing were optimal. Utilizing this functional system, we optimized the following formulation for UV curing and printing. The Ink C4 is composed of PEG-DA (92.7 wt%), a monomer that serves as the primary chain builder and flexible crosslinker, along with Irg819 (0.9 wt%) as photoinitiator. Additionally, we included DMAc (5.2 wt%) as a solvent and TEMPO-methacrylate

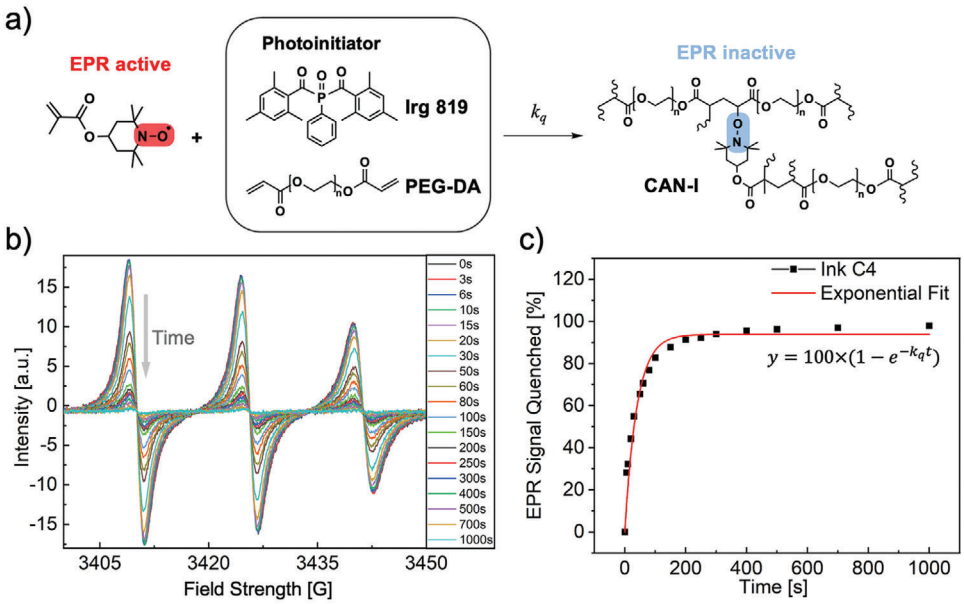

Figure 2. a) Scheme for nitroxide quenching during photoinitiated polymerization. The term "quenching" refers to the reaction of TEMPO-methacrylate with growing chains of PEG-DA, resulting in electron paramagnetic resonance (EPR) inactive alkoxyamine bonds; b) Evolution of EPR spectra during in situ irradiation of ink, ranging from 0 *s* to 1000 *s*; c) Percentage decline in the EPR signal of TEMPO-methacrylate throughout the reaction. The solid red line represents the fit using the equation: $y = 100 \times (1 - e^{-k_q t})$ with $k_q = 0.016\,s^{-1}$.

(1.2 wt%), which has a polymerizing moiety and serves as an alkoxyamine bond builder during polymerization.

Using the optimized formulation, we employed the UV curing system, resulting in a solid sample with a diameter of 19 *mm* and a thickness of 3 *mm* after 10 min of curing time at an exposure energy of 12 $mWcm^{-2}$. Subsequently, we performed experiments with 3D printing using the same formulation. A high resolution was achievable by attaining a minimum z-layer thickness of 50 µ*m* with a layer curing time of 13 *s* at an intensity of 30.0 $mWcm^{-2}$. To showcase the excellent printing quality, we designed and printed a 3D KIT-logo structure. All printed structures featured optically smooth surfaces, with hardly noticeable layer transitions. This suggests that the printing parameters were effectively optimized and the developed ink displayed good printability.

2.2. In-Depth Characterization of the Dynamic Changes

The initial covalent adaptable network (CAN-I) incorporates alkoxyamine bonds that can be thermally reactivated and used for post-polymerization via NMP in the presence of the monomer or the NER reaction with various nitroxide radicals. In this section, we perform in-depth characterizations of the dynamic modifications within the networks and identified important properties, such as the glass transition temperature, swelling degree *Q* in THF, and mesh size distribution.

For the chain extension, we have opted for styrene as monomer for two reasons. First, polystyrene exhibits significantly different mechanical properties at room temperature when compared to polyethylene glycol, which is relatively soft. Second, to the best of our knowledge, it is not feasible to use light-based techniques for the printing of polystyrene. The absorption of UV light by styrene can restrict the curing depth of the resin, potentially impacting the quality of 3D printed objects. Since nitroxide radicals are EPR active, we followed the synthesis of the CAN-I network in situ with EPR spectroscopy prior to post-synthetic modification. Accordingly, we can readily monitor the quenching of the nitroxide radical during photopolymerization. In **Figure 2b**, the EPR spectra for Ink C4 during in situ irradiation are presented, showing measurements taken at various reaction times. We observed a radical signal at 0 *s*, and its intensity declines as reaction times increase. After 1000 *s* of irradiation, the radical quenching is nearly complete (Figure 2c), as evidenced by the extremely weak signal detected in the EPR spectrum. For a clearer representation of this decline, please refer to the first integration spectra corresponding to the EPR curves in Figure S1a, Supporting Information. In addition to monitoring the quenching effect through in situ irradiation, we also explored the kinetics using EPR measurements. As depicted in Figure 2c, the data was well-fitted by an exponential decline, indicative of pseudo-first-order kinetics. This implies that the quenching rate, k_q, is linked to the concentration of nitroxide. Furthermore, the log plots of nitroxide quenching versus time over the initial 100 *s* showed a linear relationship. This allowed us to calculate the quenching rate, $k_q = 0.016\,s^{-1}$, as depicted in Figure S1b (Supporting Information).

To ensure that the detected EPR signals exclusively originate from the nitroxide radicals, we performed a control experiment under identical conditions, but in the absence of nitroxide radicals (Figure S1c, Supporting Information). The absence of any EPR signal from radicals originating from the photoinitiator (PI) suggest that its lifetime is too short for EPR detection. Consequently, it has no effect on the results of the in situ EPR analysis.

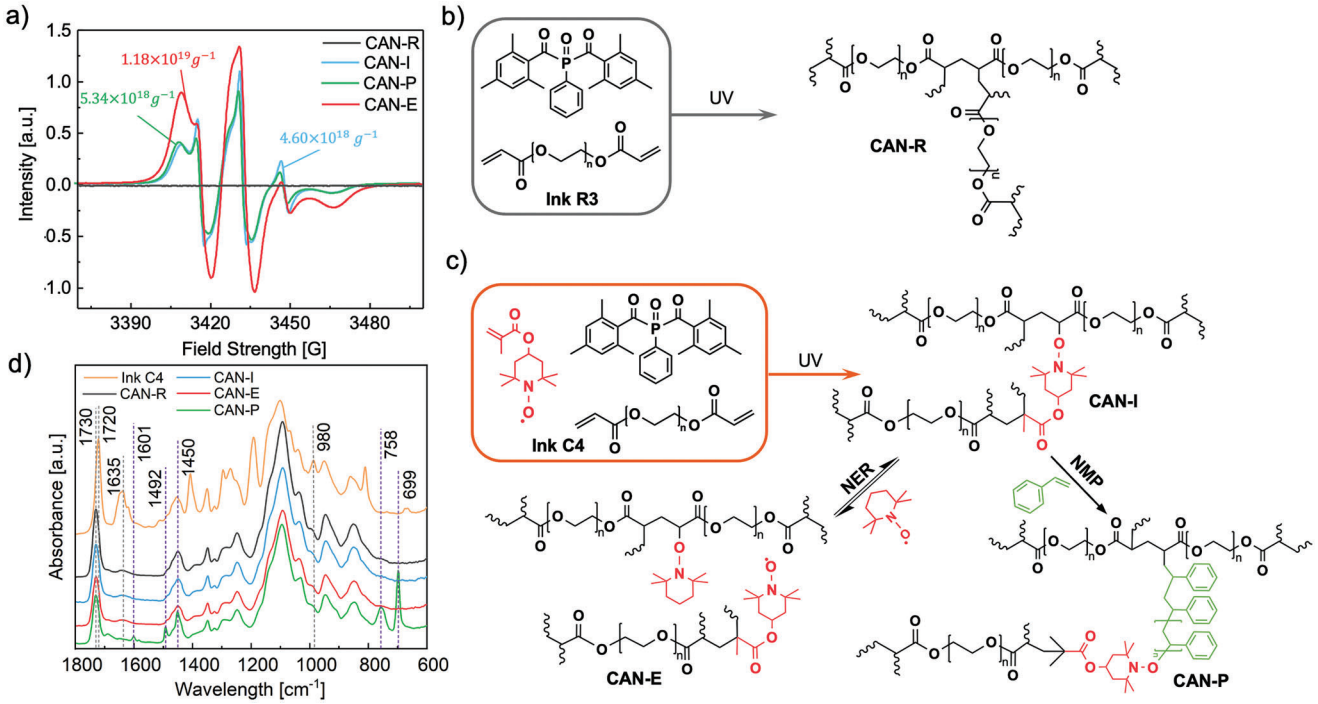

Figure 3. a) EPR spectra of the different CANs. The reference network, CAN-R, lacks nitroxide moieties and therefore shows no EPR signal. The spin density of CAN-I slightly increases after polymerization with styrene (CAN-P). As anticipated, the CAN-E structure exhibits the highest spin counts due to alkoxyamine bond disconnection through the NER reaction; b) Schematic illustration of the synthesis of CAN-R from Ink R3; c) Schematic illustration of the synthesis of CAN-I from Ink C4, along with post-synthetic modifications via nitroxide exchange reaction (CAN-E) and nitroxide-mediated polymerization (CAN-P); d) FTIR spectra comparison: Ink C4, CAN-R, CAN-I, CAN-E and CAN-P. As demonstrated, the signal corresponding to the double bond of the monomer in the ink disappeared, indicating complete polymerization after UV curing. The distinct aromatic signal of CAN-P confirms the effective post-synthetic modification with nitroxide-mediated polymerization (NMP). Prominent bands corresponding to acrylate moieties are highlighted with gray dashed lines. Noteworthy polystyrene bands are highlighted using violet dashed lines.

Furthermore, we can determine the spin density of the resultant polymer network (CAN-I) and post-modified polymer networks, CAN after NER (CAN-E) and CAN after NMP (CAN-P), using EPR spectroscopy. Additionally, we analyzed the reference network (CAN-R), which we synthesized from an ink lacking nitroxide moieties, through EPR. As shown in **Figure 3a**, after post-polymerization, the spin density in the network slightly increased from $4.60 \times 10^{18}\,g^{-1}$ to $5.34 \times 10^{18}\,g^{-1}$. By cleaving the alkoxyamine bond in the network with NER, we generated a free nitroxide radical and a carbon radical, which we combined with a mono TEMPO nitroxide radical. Releasing the free nitroxide radicals increased the spin density to $1.18 \times 10^{19}\,g^{-1}$. The EPR data collected strongly supports the proposed network structure and the postulated dynamic modifications, validating of our synthetic and modification approaches.

In the next step, we utilized fourier-transform infrared spectroscopy (ATR-FTIR) to gain insight into the acrylate conversion during photopolymerization of CANs (Figure 3b,c). The 3D CAN structures were ground and examined using FTIR analysis. Additionally, we performed FTIR analysis on reference networks (CAN-R) produced from an ink lacking TEMPO-methacrylate. We also measured the FTIR spectrum of the initial ink for comparison (Figure 3d). The unreacted monomers in the ink produced characteristic bands at 1635 and 980 cm^{-1} corresponding to the CH_2 = CH stretching vibration.[36] However, these characteristic bands were no longer visible in the ink after consumption after printing (Figure 3d). Furthermore, the distinctive absorption band at 1720 cm^{-1}, attributed to the C = O stretching vibration of the conjugated α,β-unsaturated ester, shifted to 1730 cm^{-1} for the aliphatic ester,[36] indicating the successful polymerization of both CAN-I and CAN-R. In our previous microstructure samples,[16] the observed band at 1470 cm^{-1}, assigned to the CH_3 asymmetrical bending vibration of TEMPO-methacrylate moieties, is only seen as a slight shoulder in the bulk CAN-I sample. The low amount of TEMPO species and large background signal highlights the importance of EPR spectroscopy to effectively characterize the presence of nitroxide moieties in such formulations.

It is expected that NER would result in a reduced overall crosslinking density in the resultant product (CAN-E), along with a higher overall TEMPO content compared to the initial network (CAN-I) (Figure 3c). To test this hypothesis, we subjected the 3D structure of CAN-I to heat in the presence of an excess of free TEMPO molecules and investigated it using FTIR spectroscopy. We found that, despite the NER post-synthetic modification, the CAN-I structure was preserved and that there were no significant variations in the IR spectra when comparing CAN-I and CAN-E structures (Figure 3d). However, based on the swelling test and inverse SEC analyses, we observed that CAN-E had a lower crosslinking density than CAN-I. This will be discussed below.

Furthermore, we investigated the feasibility of incorporating new monomers into the CAN-I network through controlled

NMP, utilizing the living properties of the alkoxyamine bond. We employed styrene as monomer for chain extension due to its established use in NMP.[37,38] In addition, polystyrene has markedly different mechanical properties from polyethylene glycol (PEG), the primary component of CAN-I. Unlike the rubbery PEG networks, polystyrene is glassy at ambient temperature, and we thus expect a significant increase in Young's Modulus for CAN-P relative to the initial PEG-based CAN-I at room temperature. To extend the chain of CAN-I via NMP, we immersed the 3D structures in degassed styrene, sealed the reaction vial under nitrogen, and performed the NMP at 130 °C. Confirmation of the successful incorporation of polystyrene chains into the CAN-I network by NMP chain extension was provided by the presence of polystyrene characteristic bands in the FTIR spectrum, including aromatic C = C stretching vibrations at 1601 cm^{-1}, 1492 cm^{-1}, and 1450 cm^{-1}, and C–H out-of-plane bending vibrations of aromatic rings at 758 cm^{-1} and 699 cm^{-1} (Figure 3d).

2.3. Post-Synthetic Modification of the CANs

Through extensive analysis using EPR and FTIR spectroscopy, we have conclusively confirmed the successful integration of alkoxyamine bonds into the CAN polymer networks. As previously demonstrated, this incorporation of alkoxyamine bonds enables convenient post-synthetic modifications through NMP and NER. Consequently, we observed variations in cross-linking density and the expected alteration of mesh size. To comprehensively understand the network, we present a detailed characterization that includes essential properties such as the glass transition temperature, swelling degree, and mesh size distribution.

The mesh size of CANs was determined using size-exclusion chromatography in the inverse mode (ISEC).[28,29,31,39] ISEC stands as a chromatographic method for determining the pore size distribution (PSD) of porous materials. This approach yields more pertinent insights into the characteristics of liquid chromatographic materials in situ compared to traditional methods like gas sorption and mercury intrusion.[40] Regarding the pore geometries, the interpretation of size-exclusion data into pore size pre-request an assumption about the pore shape. Simplified models of pore shapes, such as cylinders or slit-like pores, are commonly accepted as reasonable approximations for certain materials and have been utilized in pore characterization through techniques like ISEC and gas sorption methodologies.[41,42] Despite the various models available to describe pore geometries, it has been observed that ISEC is generally not very sensitive to these descriptions of pore geometry.[43,44] Consequently, the cylindrical model has been adopted nearly universally for characterizing pore size in diverse materials.[30] Unfortunately, real porous materials possess intricate structures that may not be accurately encapsulated by a few parameters. Therefore, the pore dimensions derived from ISEC should not be considered as absolute values.[45] Instead, they provide functional information on stationary phases that are particularly valuable for comparative purposes.[46] It is important to emphasize that the interpretation of the data in terms of equivalent cylindrical shape in this study serves the sole purpose of comprehending macromolecular retention and facilitating comparisons among different CAN materials.

Table 1. Summary of the key parameters for the characterization of CANs. a) Spin density, determined with solid state electron paramagnetic resonance (EPR) spectroscopy; b) Mesh size distribution (R_{ms}); c) Swelling degree (Q), calculated after 24 hours of swelling in THF; d) T_g, determined by dynamic scanning calorimetry (DSC); e) Young's Modulus, determined at a temperature of 25 °C by utilizing the stress-strain data obtained from dynamic mechanical thermal analysis (DMTA).

CANs	spin density $[g^{-1}]^{a)}$	R^1_{ms} $[nm]^{b)}$	Q $[\%]^{c)}$	T_g $[°C]^{d)}$	Young's Modulus $[MPa]^{e)}$
CAN-R	0	31.9 ± 0.1	33	−38	10.5 ± 0.3
CAN-I	4.60×10^{18}	20.7 ± 0.3	30	−36	11.7 ± 0.2
CAN-P	5.34×10^{18}	65.0 ± 0.7	102	−37	17.5 ± 0.6
CAN-E	1.18×10^{19}	48.2 ± 0.6	65	−34	8.30 ± 0.3

In our experimental setup, various CANs underwent overnight swelling in THF. Following this swelling process, the CANs were carefully positioned within a glass column equipped with adjustable pistons and densely packed until no visible gaps remained. For a comprehensive understanding of each sample, we employed a minimum of 17 different polystyrene standards, spanning a molecular weight range from 474 to 4 410 000 $gmol^{-1}$. In the case of a given CAN network, the retention times of each polymer standard were determined. Consequently, as the porosity changes, different polystyrene standards exhibit varying retention times within each network. Hence, with the known retention time and molecular weight of the utilized polystyrene standard, we can calculate the PSD of the stationary phase (i.e., CAN networks) using molecular statistical theory.[39,47,48]. This calculation is facilitated through the utilization of the commercial PoroCheck software package V2.5, developed by PSS (now Agilent) in Mainz, Germany. For further details on the adopted procedure, please refer to the Supporting Information. **Figure** 4b presents the final PSD results for various CANs. To ensure the reliability of the PSD, we conducted the analysis three times, with column repacking occurring every second measurement. To cover the wide range of pore sizes within each of the different network stationary phases, as illustrated in Figure 4a, we employed polystyrene standards spanning a broad spectrum of molecular weights. Consequently, the CAN-R network exhibited a mesh size radius of 31.9 ± 0.1 *nm*, CAN-I of 20.7 ± 0.3 *nm*, CAN-P of 65.0 ± 0.7 *nm*, and CAN-E of 48.2 ± 0.6 *nm*, respectively. For a comprehensive summary of the key parameters of the CANs, please refer to **Table 1**. Notably, we observed a consistent trend in the variation of mesh sizes across different CANs. CAN-I displayed the smallest mesh size due to the restricted chain mobility caused by the alkoxyamine moieties (Figure 4b). Conversely, CAN-E, after the nitroxide exchange reaction, had a larger mesh size as the disconnection of alkoxyamine bonds increased chain mobility (Figure 4b). The CAN-P networks had the largest mesh size. Following NMP, the main chain of CAN-P extended with polystyrene (Figure 4b), resulting in enhanced chain mobility during swelling. Moreover, the mesh size of the CANs demonstrated a clear correlation with their swelling behavior (**Figure** 5 and Table 1). Specifically, CAN-I, with the shortest mesh size, exhibited the lowest swelling degree $Q = 30\%$. In comparison, the swelling degree of the reference network, CAN-R, fell within a similar range at $Q = 33\%$ as that of CAN-I. After the NER

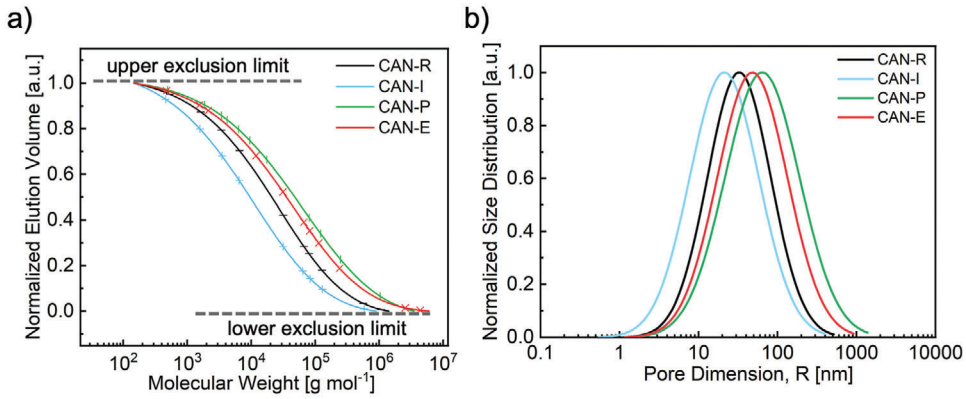

Figure 4. a) Inverse size exclusion chromatography (ISEC) showing the elution volume of polystyrene standards against their molecular weights for different CANs acting as stationary phase; b) Corresponding pore size distributions (PSD) of the different CAN networks.[39]

process, CAN-E showed a noticeable increase in its swelling degree, reaching $Q = 65\%$. On the other hand, CAN-P, with its extended polymer chain, displayed the largest swelling degree $Q = 102\%$.

To comprehensively investigate the impact on the mechanical and thermal characteristics of CAN networks, we conducted dynamic mechanical thermal analysis (DMTA) and dynamic scanning calorimetry (DSC) measurements. These techniques offered insights into properties such as Young's Modulus and the glass transition temperature (T_g). The DMTA measurements were executed on UV-cured 3D cylindrical structures (depicted in Figure 5). As we compressed the materials, they exhibited slight elastic deformation, but as the strain approached its limit, a sudden fracture occurred, leading to irreversible deformation, as illustrated in the stress–strain diagram (**Figure 6a**). The Young's Modulus was determined by calculating the slope of the linear segment in the elastic region of the stress–strain diagram. A clear difference emerged between CAN-E and the initial network CAN-I. Specifically, CAN-E displayed a reduced Young's Modulus $E = 8.3 \pm 0.3\ MPa$, in contrast to the higher value of $E = 11.7 \pm 0.2\ MPa$ observed for CAN-I (refer to Figure 6a and Table 1 for a comprehensive comparison of various CANs). This reduction in the reduced Young's Modulus can be attributed to the overall lower cross-linking density resulting from the exchange reaction. Furthermore, we investigated how the incorporation of polystyrene influenced mechanical properties through DMTA. The Young's Modulus of the CAN-P network exhibited a significant 50% enhancement compared to the initial CAN-I network ($E = 11.7 \pm 0.2\ MPa$), reaching $E = 17.5 \pm 0.6\ MPa$. This substantial increase in Young's Modulus underscores the integration of polystyrene and its impact on modulating mechanical characteristics.

Moreover, Figure 6b,c depicts the temperature-dependent behavior in compression mode, including the storage modulus (E') and the loss factor ($tan\ \delta = E''/E'$). With increasing temperature, all samples exhibit decline in the storage modulus. A distinct alteration in the E' value becomes apparent within the glassy region, particularly pronounced for the modified CANs. Upon the exchange reaction of CAN-I, CAN-E exhibits the lowest storage modulus, while CAN-P demonstrates a clearly increased storage modulus. In parallel with the Young's Modulus observations, the

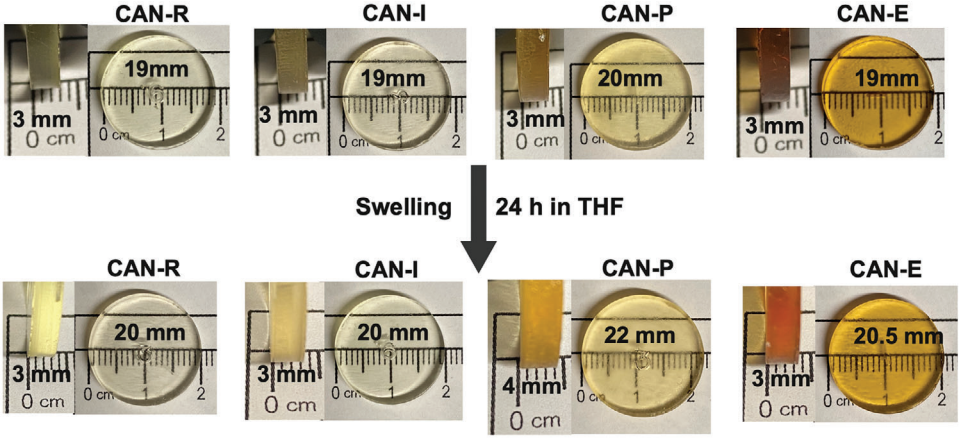

Figure 5. Swelling test of CAN-R, CAN-I, CAN-P and CAN-E. All the samples were soaked in THF for a duration of 24 hours and the swelling degree was quantified by measuring the weight of the different CANs. The networks CAN-P and CAN-E exhibited a greater capacity to absorb solvents and displayed more significant expansion when compared to both the reference (CAN-R) and initial (CAN-I) networks. Note: The dimensions displayed in the image are accurately represented; however, shadows present may lead to potential misinterpretations.

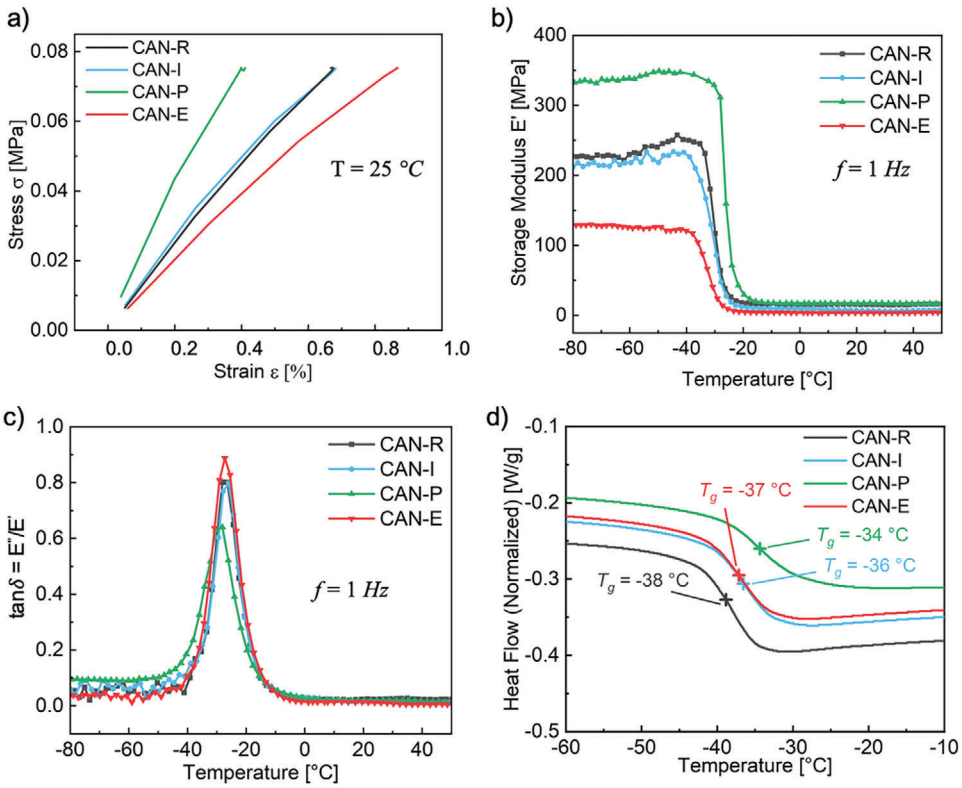

Figure 6. Mechanical and thermal properties of the bulk structure without solvent. Dynamic mechanical thermal analysis (DMTA) in compression mode was conducted over a temperature range of -100 °C to 100 °C with a rate of 2 °C min^{-1} at a frequency of 1 *Hz*. a) The stress-strain curves of CAN networks were recorded at 25 °C, employing a frequency of 1 *Hz*; b) The storage modulus was systematically compared across a range of temperatures for various CANs; c) The variation of *tan δ* in relation to temperature was measured for distinct CANs; d) Differential scanning calorimetry (DSC) outcomes revealed the glass transition temperature (T_g) of diverse CANs. The data points corresponding to the glass transition were plotted within a temperature interval of -60°C to -10°C.

variance in storage modulus underscores the prospect of tailoring mechanical properties through post-synthetic modification of CANs employing dynamic alkoxyamine bonds. Furthermore, the intensity of the maximum *tan δ* peak serves as a measure of the mobility extent of polymer chain segments at the specific temperature (Figure 6c). The network CAN-P, characterized by extended and interlaced polystyrene chains, exhibits a substantially decreased intensity. In contrast, CAN-I and CAN-R present comparable intensities, while CAN-E demonstrates elevated chain mobility due to its lower cross-linking density (Figure 3c).

Additionally, Figure 6d illustrates the spectra from the DSC measurement. The reference network, CAN-R, distinctly exhibited the lowest glass transition temperature at T_g = –38 °C, while CAN-I and CAN-E followed closely with temperatures of T_g = –36 °C and T_g = –37 °C, respectively. the network CAN-P, featuring the integration of polystyrene, presented the highest T_g at –34 °C. DSC measurements were performed in a temperature range from –80 to 130 °C, revealing a single T_g transition for each sample. This observation strongly suggests that the PEG-DA monomer experienced homogeneous polymerization under UV curing without phase separation, with the successful integration of the polystyrene chain via NMP into the CAN networks. This is further supported by the absence of the anticipated dual T_g transitions that are typically observed in materials polymerized individually. Consequently, the post-synthetic modifications present a compelling avenue for tailoring material properties, enabling precision adjustment to specific applications.

2.4. 3D DLP Printed Structures

We presented the dynamic attributes and expansion response of alkoxyamine units within more intricate 3D configurations to underscore the versatility and promise of our developed technique. Specifically, we employed the optimized mixture containing TEMPO-methacrylate to fabricate a 3D representation of the KIT logo (depicted in **Figure 7**). We printed additional KIT logos as well as gyroid structures with different size and resolution to demonstrate the versatility of this technique (See Figure S2, Supporting Information). The manufacturing of these 3D structures involved a commercial DLP printer equipped with a high-powered 385 nm UV-LED. This is evident in the smooth surface finish and imperceptible layer transitions, as illustrated in Figure 7 (CAN-I structure). In a subsequent stage, we executed the nitroxide exchange reaction by immersing the printed structure in an excess amount of TEMPO nitroxide, maintaining a temperature of 100 °C for 8 hours under nitrogen. Figure 7 illustrates the preservation of the 3D form of the printed structure following NER post-synthetic modification. Due to the

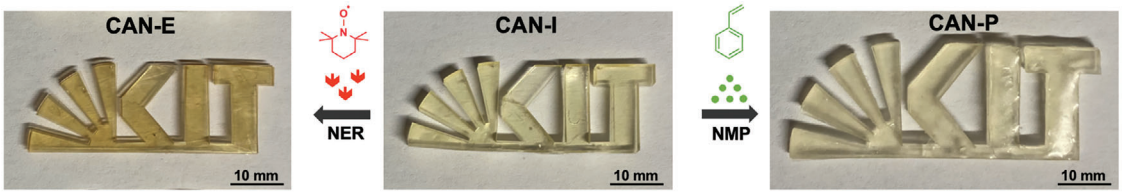

Figure 7. NER nitroxide exchange process (left) and NMP chain extension (right) of 3D printed structure with TEMPO and styrene. The top view showcases the structures of CAN-I, CAN-E, and CAN-P. The red color in CAN-E corresponds to disconnected free nitroxide radicals. Following chain extension, the KIT logo increased from $x = 42.5mm$, $y = 16.5mm$, $z = 3.29mm$ to $x = 55.3mm$, $y = 21.5mm$, $z = 4.27mm$. This demonstrates its structural integrity and displays uniform growth despite a substantial increase in volume.

release of nitroxide radicals, the structure underwent a color transformation to red. The NMP chain extension involving styrene was conducted under nitrogen at 130 °C for 24 h. As shown in Figure 7, the enlarged KIT-logo yielded a 3D structure containing polystyrene, exhibiting exceptional structural integrity despite the considerable expansion in volume. Notably, the expansion of the intricate 3D structure exhibited macroscopic uniformity. In terms of scale, the KIT-logo closely resembles the original structure, albeit with increased dimensions and enhanced rigidity.

3. Summary and Conclusion

We successfully developed a nitroxide-based ink for UV curing and DLP 3D printing of alkoxyamine containing polymer network structures. In our study, we undertook a comprehensive investigation and optimization of the 3D printing ink system. This additive manufacturing process opens up new avenues for printing dynamic and adaptive 3D polymer structures. The incorporation of dynamic alkoxyamine bonds within the printed polymer networks enables the dynamic post-printing modification of mesh size and mechanical properties through nitroxide exchange reaction and nitroxide mediated polymerization. Comprehensive characterization using inverse size-exclusion chromatography, dynamic mechanical analysis, and spectroscopic studies such as EPR and FTIR has shed light on the properties of 3D printed CANs, allowing to quantitatively monitor the dynamic changes in crosslinking degree, mesh size distribution, and mechanical properties.

Supporting Information

Supporting Information is available from the Wiley Online Library or from the author.

Acknowledgements

Christopher Klein is gratefully acknowledged for his support in the DMTA analysis of the polymer networks. E.B. acknowledges the funding from the Deutsche Forschungsgemeinschaft (DFG, German Research Foundation) under Germany's Excellence Strategy via the Excellence Cluster 3D Matter Made to Order (EXC-2082/1 - 390761711). H. M. acknowledges the University of Haute-Alsace (UHA) for the financial support from the French National Research Agency (ANR) with the reference "ANR-22-CPJ1-0077-01" and from the CNRS for a junior professorship contract. H. M. acknowledges also the financial support from the Karlsruhe Institute of Technology, in addition to the Federal Ministry of Education and Research (BMBF) and the Baden–Württemberg Ministry of Science as part of the Excellence Strategy of the German Federal and State Governments.

Open access funding enabled and organized by Projekt DEAL.

Conflict of Interest

The authors declare no conflict of interest.

Data Availability Statement

The data that support the findings of this study are available in the RADAR Research Data Repository at http://doi.org/10.35097/1896, and in the supplementary material of this article.

Keywords

3D printing, alkoxyamine dynamic bond, covalent adaptable network, nitroxide exchange reaction, nitroxide mediated polymerization

Received: December 6, 2023
Revised: February 13, 2024
Published online: March 10, 2024

[1] S. V. Murphy, A. Atala, *Nat. Biotechnol.* **2014**, *32*, 773.
[2] C. A. Spiegel, M. Hackner, V. P. Bothe, J. P. Spatz, E. Blasco, *Adv. Funct. Mater.* **2022**, *32*, 2110580.
[3] W. Zhu, X. Ma, M. Gou, D. Mei, K. Zhang, S. Chen, *Curr. Opin. Biotechnol.* **2016**, *40*, 103.
[4] B. Zhang, H. Li, J. Cheng, H. Ye, A. H. Sakhaei, C. Yuan, P. Rao, Y. Zhang, Z. Chen, R. Wang, *Adv. Mater.* **2021**, *33*, 2101298.
[5] J. Wu, J. Guo, C. Linghu, Y. Lu, J. Song, T. Xie, Q. Zhao, *Nat. Commun.* **2021**, *12*, 6070.
[6] E. Roels, S. Terryn, F. Iida, A. W. Bosman, S. Norvez, F. Clemens, G. Van Assche, B. Vanderborght, J. Brancart, *Adv. Mater.* **2022**, *34*, 2104798.
[7] S. J. Rowan, S. J. Cantrill, G. R. Cousins, J. K. Sanders, J. F. Stoddart, *Angew. Chem., Int. Ed.* **2002**, *41*, 898.
[8] C. J. Kloxin, T. F. Scott, B. J. Adzima, C. N. Bowman, *Macromolecules* **2010**, *43*, 2643.
[9] X. Kuang, D. J. Roach, J. Wu, C. M. Hamel, Z. Ding, T. Wang, M. L. Dunn, H. J. Qi, *Adv. Funct. Mater.* **2019**, *29*, 1805290.
[10] Z. Fang, Y. Shi, H. Mu, R. Lu, J. Wu, T. Xie, *Nat. Commun.* **2023**, *14*, 1313.
[11] X. Shi, J. Zhang, N. Corrigan, C. Boyer, *Polym. Chem.* **2022**, *13*, 44.
[12] A. Bagheri, H. Ling, C. W. A. Bainbridge, J. Jin, *ACS Appl. Polym. Mater.* **2021**, *3*, 2921.

[13] C. Cui, L. An, Z. Zhang, M. Ji, K. Chen, Y. Yang, Q. Su, F. Wang, Y. Cheng, Y. Zhang, *Adv. Funct. Mater.* **2022**, *32*, 2203720.
[14] Q. An, I. D. Wessely, Y. Matt, Z. Hassan, S. Bräse, M. Tsotsalas, *Polym. Chem.* **2019**, *10*, 672.
[15] Y. Jia, Y. Matt, Q. An, I. Wessely, H. Mutlu, P. Theato, S. Bräse, A. Llevot, M. Tsotsalas, *Polym. Chem.* **2020**, *11*, 2502.
[16] Y. Jia, C. A. Spiegel, A. Welle, S. Heißler, E. Sedghamiz, M. Liu, W. Wenzel, M. Hackner, J. P. Spatz, M. Tsotsalas, E. Blasco, *Adv. Funct. Mater.* **2022**, *33*, 2207826.
[17] H. Otsuka, K. Aotani, Y. Higaki, Y. Amamoto, A. Takahara, *Macromolecules* **2007**, *40*, 1429.
[18] L. Tebben, A. Studer, *Angew. Chem., Int. Ed.* **2011**, *50*, 5034.
[19] B. Schulte, M. Tsotsalas, M. Becker, A. Studer, L. De Cola, *Angew. Chem., Int. Ed.* **2010**, *49*, 6881.
[20] H. Otsuka, *Polym. J.* **2013**, *45*, 879.
[21] K. Jin, L. Li, J. M. Torkelson, *Adv. Mater.* **2016**, *28*, 6746.
[22] O. Ouari, D. Gigmes, *Nitroxides: Synthesis, Properties and Applications*, Royal Society of Chemistry, London, UK **2021**.
[23] G. Audran, E. G. Bagryanskaya, R. Bikanga, M. L. Coote, O. Guselnikova, C. L. Hammill, S. R. Marque, P. Mellet, P. S. Postnikov, *Prog. Polym. Sci.* **2023**, *144*, 101726.
[24] I. Wagner, S. Spiegel, J. Brückel, M. Schwotzer, A. Welle, M. H. Stenzel, S. Bräse, S. Begum, M. Tsotsalas, *Macromol. Mater. Eng.* **2023**, *308*, 2300048.
[25] L. Li, X. Chen, K. Jin, M. B. Rusayyis, J. M. Torkelson, *Macromolecules* **2021**, *54*, 1452.
[26] I. Wessely, V. Mugnaini, A. Bihlmeier, G. Jeschke, S. Bräse, M. Tsotsalas, *RSC Adv.* **2016**, *6*, 55715.
[27] Y. Jia, G. Delaittre, M. Tsotsalas, *Macromol. Mater. Eng.* **2022**, *307*, 2200178.
[28] M. Briššová, M. Petro, I. Lacık, A. Powers, T. Wang, *Anal. Biochem.* **1996**, *242*, 104.
[29] M. Goto, B. J. McCoy, *Chem. Eng. Sci.* **2000**, *55*, 723.
[30] P. DePhillips, A. M. Lenhoff, *J. Chromatogr. A* **2000**, *883*, 39.
[31] C. Pfeifer, F. Cavalli, B. Huber, P. Theato, L. Barner, M. Wilhelm, *Macromol. Chem. Phys.* **2021**, *222*, 2000300.
[32] T. Wu, P. Jiang, Z. Ji, Y. Guo, X. Wang, F. Zhou, W. Liu, *Macromol. Mater. Eng.* **2020**, *305*, 2000397.
[33] J. Zhang, P. Xiao, *Polym. Chem.* **2018**, *9*, 1530.
[34] X. Peng, L. Yue, S. Liang, S. Montgomery, C. Lu, C. Cheng, R. Beyah, R. R. Zhao, H. J. Qi, *Adv. Funct. Mater.* **2022**, *32*, 2112329.
[35] J. Moon, Y. Shul, H. Han, S. Hong, Y. Choi, H. Kim, *Int. J. Adhes. Adhes.* **2005**, *25*, 301.
[36] J. M. Thompson, *Infrared Spectroscopy*, Pan Stanford Publishing, Singapore **2018**.
[37] J. Nicolas, Y. Guillaneuf, C. Lefay, D. Bertin, D. Gigmes, B. Charleux, *Prog. Polym. Sci.* **2013**, *38*, 63.
[38] R. B. Grubbs, *Polym. Rev.* **2011**, *51*, 104.
[39] A. Gorbunov, L. Y. Solovyova, V. Pasechnik, *J. Chromatogr. A* **1988**, *448*, 307.
[40] Y. Yao, A. M. Lenhoff, *J. Chromatogr. A* **2004**, *1037*, 273.
[41] L. Z. Vilenchik, J. Asrar, R. C. Ayotte, L. Ternorutsky, C. J. Hardiman, *J. Chromatogr. A* **1993**, *648*, 9.
[42] S. Figueroa-Gerstenmaier, J. Bonet Avalos, L. D. Gelb, K. E. Gubbins, L. F. Vega, *Langmuir* **2003**, *19*, 8592.
[43] J. H. Knox, H. P. Scott, *J. Chromatogr. A* **1984**, *316*, 311.
[44] W. Yau, J. Kirkland, D. Bly, H. Stoklosa, *J. Chromatogr. A* **1976**, *125*, 219.
[45] L. Hagel, M. Östberg, T. Andersson, *J. Chromatogr. A* **1996**, *743*, 33.
[46] P. DePhillips, A. M. Lenhoff, *J. Chromatogr. A* **2001**, *933*, 57.
[47] E. F. Casassa, *J. Polym. Sci. Part B: Polym. Lett.* **1967**, *5*, 773.
[48] E. F. Casassa, Y. Tagami, *Macromolecules* **1969**, *2*, 14.

